

Structural Characterization of Nanoparticle-Supported Lipid Bilayer Arrays by Grazing Incidence X-ray and Neutron Scattering

Nicolò Paracini,* Philipp Gutfreund, Rebecca Welbourn, Juan Francisco Gonzalez-Martinez, Kexin Zhu, Yansong Miao, Nageshwar Yepuri, Tamim A. Darwish, Christopher Garvey, Sarah Waldie, Johan Larsson, Max Wolff, and Marité Cárdenas*



Cite This: *ACS Appl. Mater. Interfaces* 2023, 15, 3772–3780



Read Online

ACCESS |



Metrics & More



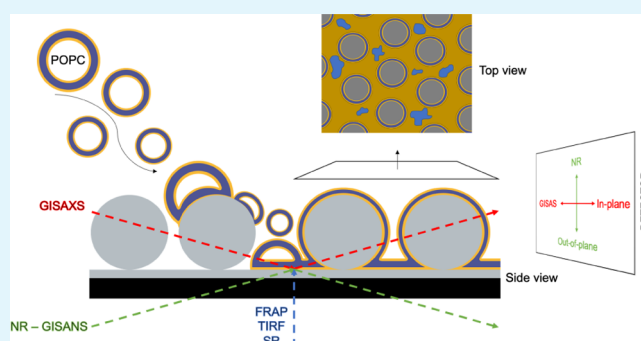
Article Recommendations



Supporting Information

ABSTRACT: Arrays of nanoparticle-supported lipid bilayers (nanoSLB) are lipid-coated nanopatterned interfaces that provide a platform to study curved model biological membranes using surface-sensitive techniques. We combined scattering techniques with direct imaging, to gain access to sub-nanometer scale structural information on stable nanoparticle monolayers assembled on silicon crystals in a noncovalent manner using a Langmuir–Schaefer deposition. The structure of supported lipid bilayers formed on the nanoparticle arrays via vesicle fusion was investigated using a combination of grazing incidence X-ray and neutron scattering techniques complemented by fluorescence microscopy imaging. Ordered nanoparticle assemblies were shown to be suitable and stable substrates for the formation of curved and fluid lipid bilayers that retained lateral mobility, as shown by fluorescence recovery after photobleaching and quartz crystal microbalance measurements. Neutron reflectometry revealed the formation of high-coverage lipid bilayers around the spherical particles together with a flat lipid bilayer on the substrate below the nanoparticles. The presence of coexisting flat and curved supported lipid bilayers on the same substrate, combined with the sub-nanometer accuracy and isotopic sensitivity of grazing incidence neutron scattering, provides a promising novel approach to investigate curvature-dependent membrane phenomena on supported lipid bilayers.

KEYWORDS: nanoparticle-supported lipid bilayers, nanoSLB, membrane curvature, model membranes, neutron reflectometry, GISANS, GISAXS



INTRODUCTION

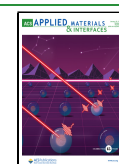
Supported lipid bilayers (SLBs) are robust and widespread models of biological membranes with applications ranging from biophysical studies of membrane function¹ to biosensing.² Planar SLBs typically consist of phospholipid bilayers formed via vesicle fusion,³ solvent-assisted bilayer formation,⁴ or Langmuir–Blodgett and Langmuir–Schaefer monolayer transfer techniques^{5,6} onto flat hydrophilic interfaces of materials like quartz, mica, and silicon oxide. The wide variety of model cell membranes available for biophysical research offer a plethora of possible approaches to study the different aspects of membrane bioscience that are often too complex to address directly on the natural cell envelope, such as lipid–lipid and protein–lipid interactions.¹ The effect of membrane morphology on the functional and structural properties of the lipid and protein components of plasma membranes is one of the aspects that remains more elusive, partly due to the scarcity of suitable model membrane systems. Membrane curvature has been shown to affect lipid and protein sorting and segregation^{7,8} in processes that contribute to vital functions

of cells such as cell division and membrane remodeling.^{9–11} A well-characterized example of curvature-dependent lipid segregation is the preferential partition of the cone-shaped lipid cardiolipin into regions of negative curvature such as those found at the polar regions of rod-shaped bacteria^{12,13} and in the lumen-facing leaflet of mitochondrial cristae.¹⁴ Experiments on model lipid bilayers have shown that when cardiolipin is incorporated into large unilamellar vesicles of 100 nm in diameter, cardiolipin molecules display a 4:1 preference for the inner leaflet of the liposomes,¹⁵ and this degree of curvature is in turn able to modulate cardiolipin binding to cytochrome c.¹⁶ Most curvature-dependent lipid

Received: October 21, 2022

Accepted: December 29, 2022

Published: January 10, 2023



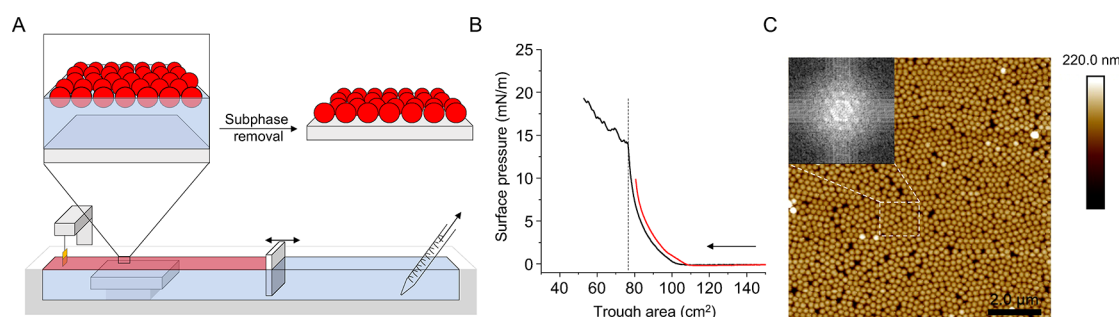


Figure 1. Langmuir–Schaefer transfer of a NP monolayer onto a solid substrate. (A) Schematic representation of the modified Langmuir–Schaefer transfer of the silica NP monolayer onto a submerged silicon crystal. Once the NP monolayer (red area) was compressed to the target surface pressure, measured by the Wilhelmy plate, the aqueous subphase was slowly removed from behind the barrier using a serological pipette tip connected to a pump. (B) Pressure–area isotherm of NP monolayer compressed above (black) and below (red) the collapse point at 15 mN/m and indicated by an abrupt change in the slope (dashed line); the arrow indicates the direction of compression. (C) NP monolayer (nominal diameter 2000 Å) after transfer onto a silicon wafer imaged by AFM. Black areas correspond to gaps between the particles, while bright spots are particles absorbed on top of the NP monolayer. The scale bar is 2 μm. The inset shows a Fourier transform of the highlighted region in the AFM image and the corresponding hexagonal lattice.

segregation studies rely on fluorescence microscopy and the use of fluorophores which are either covalently linked to or preferentially interact with target lipid molecules to track and visualize. Lipids preference for a certain type of curvature is highly dependent on molecular shape, which can easily be altered by the steric hindrance of covalently linked fluorescent probes while the use of added fluorescent stains has led to debates around their target specificity in membrane curvature studies.¹⁷ Deuterium labeling, in combination with isotope-sensitive neutron scattering techniques, represents a promising and complementary alternative to fluorescent labels that largely preserves the molecular shape of lipids and enables structural studies with sub-nanometer accuracy of model membranes with complex morphologies.

There is growing interest toward the development of nonplanar SLBs that deviate from canonical flat interfaces and instead display a degree of curvature of the lipid bilayer, recreating morphological aspects of the cell surface, which can display a wide range of degrees of curvature. These model systems find applications in the study of membrane curvature-mediated phenomena such as lipid and protein segregation and binding of curvature-sensitive proteins.^{7,18–23} For this purpose, nano- and micropatterned surfaces represent attractive substrates for the formation of SLBs with a well-defined surface morphology imparted by the underlying interfacial nanostructure. Both top-down and bottom-up methods have been adopted for the modification of flat interfaces and the formation of surface patterns suitable to form curved SLBs. Several top-down approaches rely on nanolithography techniques, which afford a high degree of control and fine-tuning over the resulting surface structure.^{7,19} The high precision of top-down methods however often comes at the cost of time and resources, which can become limiting factors when dealing with large surfaces and number of substrates to functionalize. Bottom-up approaches, on the other hand, typically rely on self-assembly processes driven by chemical and physical forces and can be exploited to fabricate patterned samples using nanoparticles (NP) to serve as substrates for SLB formation.^{18,20,24} Among bottom-up methods employed to form large arrays of NPs, Langmuir–Blodgett and Langmuir–Schaefer depositions offer an additional level of control on the self-assembly process by enabling the adjustment of the packing density of the Langmuir monolayer

at the air/water interface prior to its transfer onto a solid substrate.^{25–27} Furthermore, Langmuir transfer techniques have the advantage of yielding large uniform monolayers, which make well-suited samples for characterization by flux-limited grazing incidence scattering methods such as neutron reflectometry (NR) and grazing incidence neutron small-angle scattering (GISANS).^{28,29} Due to their unique ability to probe noninvasively buried interfaces and their differential sensitivity toward hydrogen and deuterium, neutrons are among the most powerful surface-sensitive techniques for the structural characterization of complex biological thin films at solid/liquid interfaces, of which SLBs represent a primary example. Grazing incidence neutron scattering, particularly NR, has found wide application in the structural characterization of planar SLBs; however, the potential of techniques like GISANS, as well as NR, remains largely untapped when it comes to structural studies of model membranes with a more complex morphology. In this context, NR and GISANS, combined with selective lipid deuteration, can provide a novel approach to study the effect of curvature on the in-plane and out-of-plane structural features of SLBs.

In this article, we exploit a modified Langmuir–Schaefer deposition method to form large arrays of spherical silica NP on silicon oxide surfaces that are used as substrates to form nanoparticle-supported lipid bilayers (nanoSLB). First, we combine grazing incidence X-ray and neutron scattering to probe the structure of the NP arrays in both dry and aqueous environments (i.e., at the solid/air and solid/liquid interface). The formation of lipid bilayers via vesicle fusion on the nanoparticle arrays, investigated by quartz crystal microbalance with dissipation (QCMD) and fluorescence microscopy, indicates that lipids fuse on the substrate to form a lipid bilayer that retains lateral mobility. Finally, the in-plane and out-of-plane structural features of the nanoSLB system are resolved by NR and corroborated by GISANS revealing the formation of both a curved lipid bilayer coating the spherical particles as well as a planar bilayer on the underlying flat substrate, highlighting the coexistence of flat and curved regions.

RESULTS AND DISCUSSION

The formation of densely packed arrays of nonporous silica NPs was achieved via a modified Langmuir–Schaefer transfer

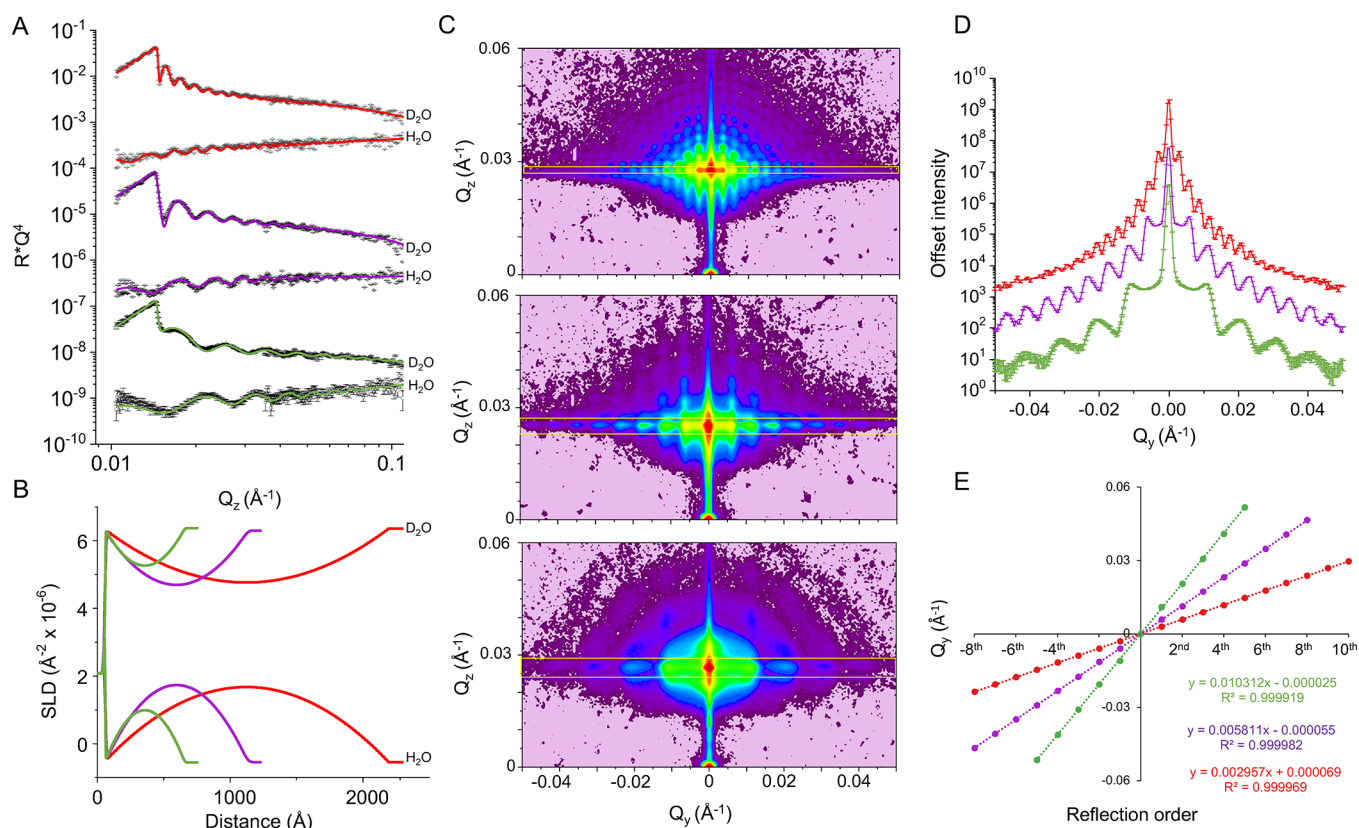


Figure 2. Structural characterization of NP monolayers by NR and GISAXS (A) Neutron reflectometry data (points) and best fit (lines) of three monolayers containing NP of different sizes, measured in D_2O and H_2O . Data and corresponding fits are offset vertically for clarity. (B) Corresponding SLD profile derived from the constrained fit of NR data from the two solution isotopic contrasts for each NP set. (C) GISAXS detector images of three monolayers measured at the air/solid interface. (D) Plot of the integrated intensities within the yellow boxes shown in (C). Absolute intensity is offset for clarity. (E) Linear regressions of the maxima positions along Q_y of the peaks shown in (D) displaying the equations of the fits and the R^2 values. The x coefficient in the equations corresponds to the average separation of the peaks, ΔQ_y .

of NPs from the air/water interface onto a pre-submerged polished silicon substrate,^{30,31} as depicted in Figure 1A. To maximize the particle density in the monolayer, pressure–area isotherms were recorded to establish the maximum surface pressure applicable to the NP monolayer at the air–water interface before excessive compression resulted in a collapse, indicated by an abrupt change in surface pressure. A value slightly below the collapse pressure was selected for NP depositions (Figure 1B). Atomic force microscopy (AFM) confirmed the formation of an NP layer with a high density of particles packed in a hexagonal lattice and interspersed with minor defects (Figure 1C).

Imaging techniques, such as AFM, only provide local information over small regions. Scattering methods, on the other hand, can probe the average structure over the large areas obtained using the Langmuir–Schaefer assembly method, providing information on the structure of complex thin films in both dry and aqueous environments.

X-ray and Neutron Characterization of NP Monolayers. Following the assembly method illustrated in Figure 1, monolayers of commercial NP with nominal diameters of 50, 100, and 200 nm were prepared and characterized by NR and GISAXS at the solid/liquid and air/solid interfaces (Figure 2). The samples, assembled into custom-built solid/liquid cells, were characterized by NR in an aqueous environment. NR measurements enable the determination of the structure of buried thin films along the axis perpendicular to the substrate, yielding a profile describing the scattering length density

(SLD) distribution, which determines the neutron refractive index along the normal to the surface. Reflectivity curves measured in the presence of H_2O and D_2O were fitted simultaneously to a model of the interface describing a monolayer of spheres as detailed in the Supporting Information and Figure S1. The SLD profiles obtained from the constrained fits to the reflectivity curves collected in H_2O and D_2O yielded NP monolayer thicknesses of ~ 2146 , ~ 1088 , and ~ 602 Å for the three samples (Table S1), in good agreement with the nominal size of the particles and the sizes obtained from dynamic light scattering (DLS) measurements (Figure S2), confirming the formation of NP monolayers (Figures 2A and S3). The in-plane packing density of the particles in the monolayers was extracted from the contrast provided by the hydrogenous and deuterated aqueous solutions and was found to be $\sim 66\%$ for the largest particles, $\sim 61\%$ for the intermediate size, and $\sim 42\%$ for the smallest NPs (Table S1), where a value of 100% in the model corresponds to a defect-free layer of spheres ideally packed in a hexagonal lattice. The significantly worse packing of the smallest particles is indicative of larger areas occupied by defects in the NP monolayer, which might result from a size-dependent tendency to form inhomogeneous aggregates during the drying step following the Langmuir–Schaefer procedure. DLS showed a higher polydispersity for the smallest particles compared to the larger 100 and 200 nm NPs, which might have contributed to hindering ideal hexagonal packing; however, even for the 50 nm particles,

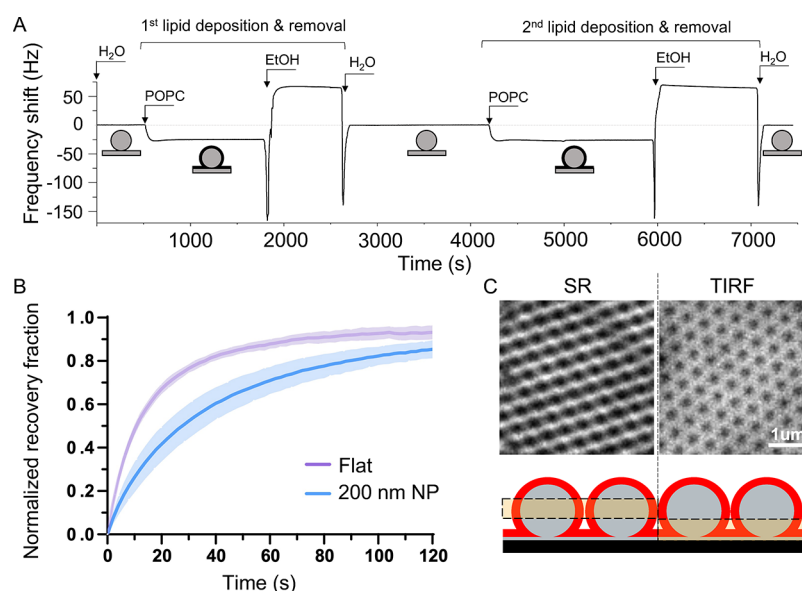


Figure 3. Formation of nanoSLB measured by QCMD and fluorescence microscopy. (A) QCMD trace monitoring the deposition of POPC onto a silica sensor coated with a monolayer of NP. Labels indicate the injection of different solutions in the QCMD flow module. The light gray flat dotted line is a guide to the eye set at zero Hz frequency shift, showing that lipids can be deposited and removed without affecting the NP layer. (B) Recovery of the fluorescence intensity after photobleaching showing the average of different measurements from five different regions of interest with the standard deviation represented by the shaded area. (C) Super-resolution (SR) microscopy and total internal reflection fluorescence (TIRF) images of NP array coated with a POPC bilayer; the highlighted boxes in the cartoon show the regions where each fluorescence microscopy technique is most sensitive. In SR and TIRF imaging, images were acquired on nanoSLB formed on particles with a larger nominal diameter (400 nm) that provides the optimal resolutions for the SLBs at different Z-positions in the focal plane.

polydispersity index remained below 0.1, indicating a highly monodisperse population.

To complement the structural information obtained by NR, the NP arrays were investigated by GISAXS, which is sensitive to the in-plane arrangement and correlations between the NPs.³² All three particle sizes gave rise to a strong GISAXS signal displaying several orders of well-defined peaks resulting from the scattering produced by the particle arrays (Figure 2C). The intensity and Q spacing of the peaks encodes information on the size and shape of the particles in the array, according to the inverse relationship between the Q_y spacing of the maxima and the corresponding real-space structures that generated them, according to $d = 2\pi/\Delta Q_y$. The average in-plane correlation distances related to the patterns observed were calculated from the Q_y spacing of the peaks in each sample. Signals were integrated across the horizontal Q_y axis and over a Q_x range corresponding to the angle of specular reflection, adjusted to include a single row of peaks in each integration box (Figure 2D, integrated regions shown by the yellow boxes in Figure 2C). The linear plot of the Q_y position of the maxima against the order of the peaks shows that the maxima are equidistant in Q_y , and the slope of the straight lines fitted through the data points (the m factor in the line equation $y = mx + c$) corresponds to the average ΔQ_y (Figure 2E). The slopes obtained from the different samples yielded correlation distance values of 2124, 1081, and 609 Å for the three particles analyzed, in close agreement with the monolayer thickness values extracted from NR and the values obtained by DLS, indicating that the correlation distances obtained from the model-independent analysis of the GISAXS scattering patterns contain information on the form factor of the particles.

Using the information on particle size obtained from NR measurements, simulated GISAXS signals were generated using the BornAgain software³³ that implements the distorted wave

Born approximation framework to calculate the scattering signal from an ensemble of particles on a surface (Figure S4). The average lattice distances, the distance between the centers of the spheres, used in the simulations were 620, 1100, and 2190 Å for the three sizes, and lower densities of spheres were assumed as the size of the particles decreased (Table S2), following the trend observed in the NR data. The simulated scattering was overall in good agreement with the data, although providing only qualitative information on the average lattice distances and particle densities as the values displayed were not extracted from a fitting routine as in the case of the NR data.

NanoSLB Formation by QCMD and Fluorescence Microscopy. The monolayers containing the largest NP displayed the highest particle density and were therefore chosen as the substrate for the study of lipid bilayer deposition. Lipid deposition via vesicle fusion was monitored by QCMD, which was used to compare the process of bilayer formation on conventional “flat” silicon oxide sensors and on sensors coated with the 200 nm NP monolayer (Figure 3A). The frequency shift (Δf) observed after injecting POPC vesicle and rinsing with water was -24.2 ± 0.7 and -25.5 ± 0.8 Hz on the flat and NP-coated sensors respectively, in line with the values reported previously for the formation of lipid bilayers on flat silicon oxide sensors as well as on QCMD sensors coated with NP.¹⁸ The shift in dissipation (ΔD) amounted to $+0.4 \pm 0.3$ ppm on the flat and -5.8 ± 1.2 ppm on the NP-coated surfaces (Figure S5A). The slightly higher Δf value recorded on the NP sample shows a marginally higher amount of lipids adsorbed while the negative ΔD indicates that lipid addition affects the properties of the NP layer, suggesting that intercalation of lipids in between the NP increases the overall stiffness of the nanoSLB layer.³⁴ The surfaces were then rinsed with ethanol to remove the POPC, which in both cases caused

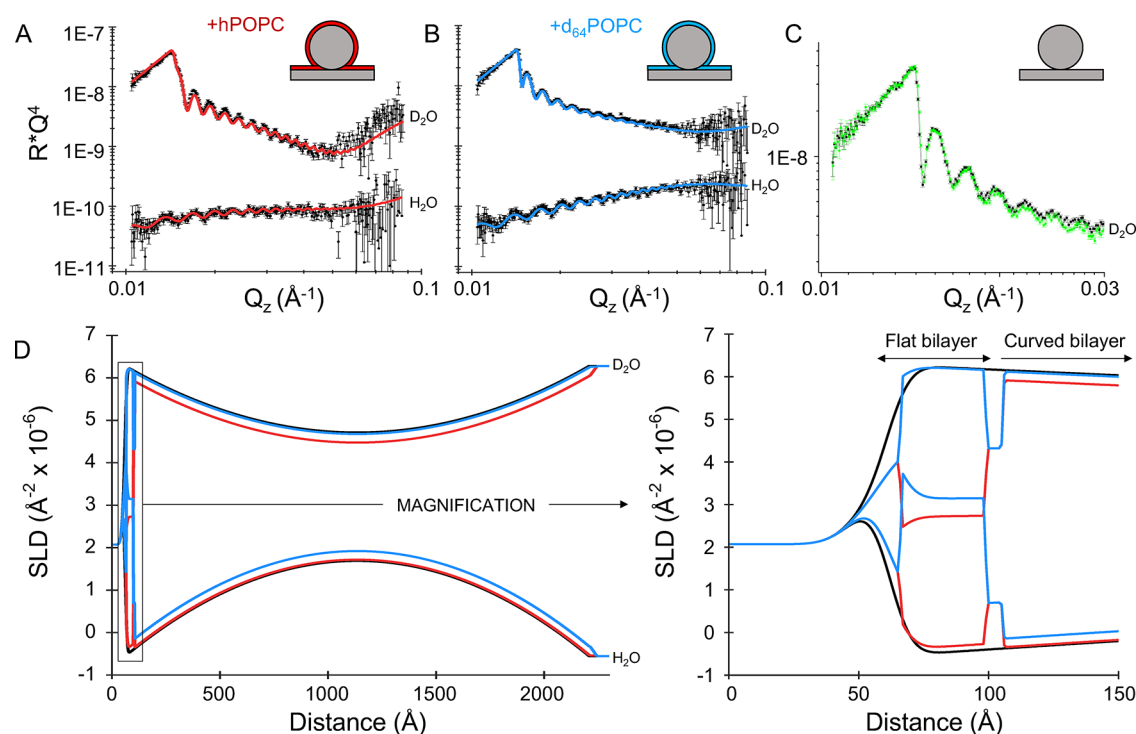


Figure 4. Vertical structure of the lipid-coated NP array. (A) NR data (points) and best fit (red lines) of nanoSLB formed with hPOPC in H₂O and D₂O. (B) NR data (points) and best fit (blue lines) of the nanoSLB formed with d₆₄POPC in H₂O and D₂O. (C) NR data from NP monolayer in D₂O before (black) and after (green) one cycle of lipid deposition and removal, showing recovery of the reflectometry signal upon EtOH rinsing. (D) SLD profiles describing the NP monolayer in the absence of lipids (black dashed lines) in the presence of hPOPC (red lines) and in the presence of d₆₄POPC (blue lines) obtained from the constrained fits with six datasets, parameters of the fits are shown in Table S3. The expanded region shows a magnification of the flat SiO₂ interface highlighting the formation of the planar SLB on the flat silicon substrate.

Δf and ΔD to return to the baseline measured at the beginning of the experiment, indicating complete removal of the lipids by the ethanol wash, with the NP array remaining unperturbed. A second cycle of lipid deposition and removal was carried out yielding Δf and ΔD values in line with the shifts observed in the first cycle, showing full reusability of the NP array as a substrate for the formation of nanoSLBs (Figure 3A). The diffusivity of the POPC molecules within the nanoSLB was investigated using fluorescence recovery after photobleaching (FRAP). Compared to SLB formed onto flat glass surfaces, the measured lipid diffusion after bleaching was slower on the bilayers assembled on the NP-coated substrate (Figure 3B). The final recovery was nonetheless comparable between the two substrates after 120 s from the bleaching (Figure S5B), indicating that lipid mobility in the nanoSLB, although more restricted, was still largely retained both in the planar bilayer and around the NP. Further experiments are required to understand to what extent diffusion takes place directly between neighboring NPs compared to diffusion mediated by the planar underlying SLB. Imaging of the nanoSLB by super-resolution (SR) and total internal reflection fluorescence (TIRF) microscopy provided a clear picture of the fluorescent bilayer and the NP array. The intense fluorescence in the TIRF signal suggests the presence of a lipid bilayer coating the area in between the particles on the flat substrate while the fluorescence signal in SR, which comes from higher up in the sample, indicates the presence of a ring of lipids around the particles (Figure 3C).

Structure of NanoSLB by Specular NR. To access information on the structure of the lipid bilayer formed on the NP array, the nanoSLB was characterized by NR. To fully

exploit the ability of neutrons to differentiate between hydrogenous and deuterated molecules, the process investigated by QCMD (Figure 3A) was replicated on the neutron beam line using first hydrogenous hPOPC, followed by regeneration of the surface with ethanol and deposition of tail deuterated d₆₄POPC. After each lipid assembly, the sample was characterized both in H₂O and in D₂O. The reflectivity datasets collected in H₂O and D₂O on the bare NP array, the hydrogenous nanoSLB, and the deuterated nanoSLB were then fitted to a common model of the interface where the structural parameters describing the SiO₂ NP monolayer were shared across the six conditions, while the SLD of the lipids and their volume fractions were allowed to vary (see Figure 2D,E for the fits and SLD of the NP monolayer before lipids addition). The model that produced the most accurate fit to the reflectivity data from the nanoSLB samples included a lipid bilayer coating the entire nanoparticle surface as well as part of the flat surface of the silicon substrate supporting the particles, as suggested by the fluorescence microscopy data (see the Supporting Information and Figure S1 for a detailed description of the model used). Addition of hPOPC vesicles to the NP array caused a prominent shift of the reflectivity profile measured in D₂O while leaving the signal recorded in H₂O mostly unaffected, as expected from the deposition of hydrogenous material at the interface (Figure S6A). Conversely, addition of d₆₄POPC resulted in a large shift in the reflectivity measured in H₂O but no significant changes in D₂O (Figure S6B). Similarly to that observed with QCMD, rinsing the nanoSLB with ethanol between bilayer depositions reverted the reflectivity back to the initial profile measured before lipid addition,

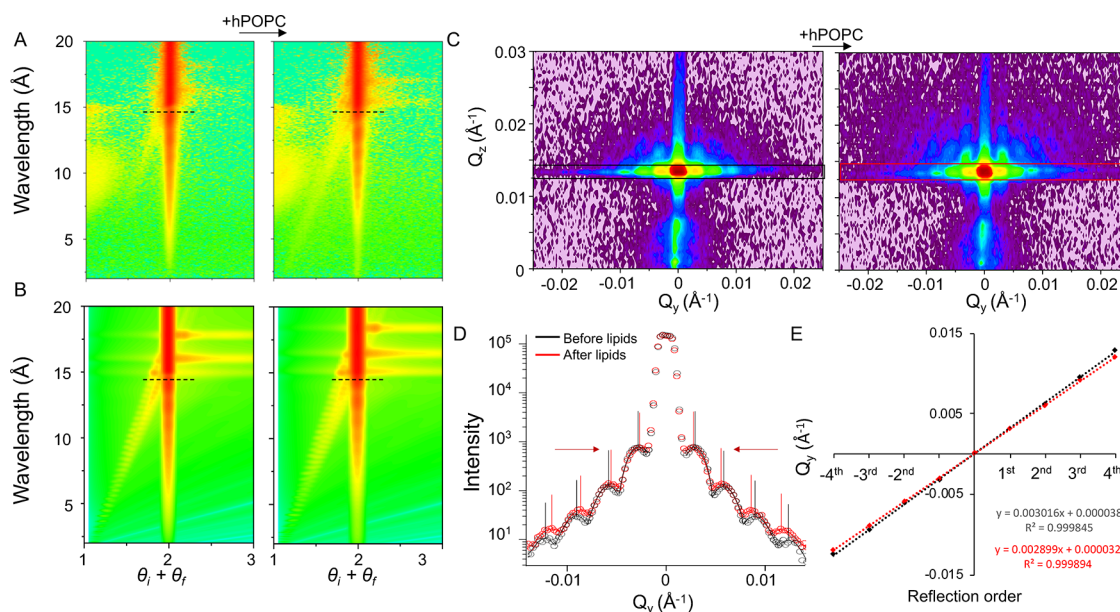


Figure 5. Effect of NanoSLB formation on GISANS and off-specular NR signals. (A) Off-specular NR data in D₂O before (left) and after (right) the addition of hPOPC to the NP array (dashed lines indicate the position of the critical edge). (B) Simulations of off-specular NR in the absence (left) and presence (right) of lipids coating the NP; θ_i and θ_r are the incident and reflected angles, respectively. (C) GISANS detector images of NP monolayer in D₂O before (left) and after (right) the addition of hPOPC. (D) Integration across Q_y of the GISANS images corresponding to the colored boxes in (C) before (black) and after (red) addition of lipids. Black and red vertical lines indicate the maxima position of individual gaussian curves fitted to the peaks, and red arrows indicate the direction of these peaks shift upon lipid addition. (E) Linear fits to the maxima positions along Q_y of the peaks before (black) and after (red) formation of hPOPC nanoSLB shown in (D). The equations of the fits and the R^2 values are displayed in the graph. The x coefficient in the equations corresponds to the average separation of the peaks, ΔQ_y .

confirming nearly complete removal of lipids while preserving the intact NP monolayer structure (Figure 4C).

Both the hydrogenous and the deuterated systems were described using the same set of shared parameters for thickness and hydration, with the only difference being the SLD of the lipid tails. The parameters obtained from the fits to the NR data described the formation of a lipid bilayer adhering to the NP, which coated the entire surface of the spheres with a high coverage as indicated by the low volume fraction of water detected in the tail region, below 1% (Table S3 and Figure S7). Additionally, a planar lipid bilayer formed on the silicon crystal surface underlying the NP monolayer, with an overall coverage of $\sim 55\%$, indicating the formation of a less complete lipid layer in comparison with the bilayer coating the NP. On planar SiO₂ surfaces, vesicles tend to fuse into high-coverage SLBs once a critical surface density of intact vesicles is reached,^{35–37} whereas this accumulation process is not required on the surface of SiO₂ NP, where vesicles have been suggested to fuse one by one as indicated by cryo-electron microscopy images.³⁸ The lower coverage of the underlying planar SLB is likely to result from the hindrance of the large NP which interfered with the accumulation of vesicles that leads to the formation of homogeneous and continuous lipid bilayers, resulting in a suboptimal coverage. Along with the differences in coverage, the structural data revealed an overall ~ 9 Å thinner nanoSLB (~ 37 Å) compared to the planar bilayer (~ 46 Å). Although both tails and headgroup thickness parameters obtained from the error analysis displayed an overlap of the confidence interval regions as displayed by their posterior distributions (Figure S7), a comparable difference was recently also reported on a similar system studied by NR by Armanious et al.³⁹ While the parameters obtained for the planar POPC SLB are in excellent agreement with previously reported values,^{40,41} the

values obtained for the thickness of the nanoSLB seem to indicate a suboptimal packing of the lipids around the spheres that could have resulted from the curvature imparted by the NP substrate. Results on bilayer thickness estimates obtained from SANS on POPC vesicles of varying size in bulk do not show significant thickness differences between vesicles in this size range.⁴² Therefore, the effect observed on the structure of the nanoSLB is likely to be a consequence of the interaction with the NPs and their surface chemistry, possibly due to differences in the overall density of silanol groups or differences in roughness between the planar SiO₂ substrate and the NP SiO₂ interface. Additionally, it has to be noted that the thickness of the nanoSLB is not directly measured by NR but is extracted from the volume fraction contributions of the nanoSLB to the SLD of the slices used to model the interface as described in the Supporting Information. The NR data yielded comparable results in terms of differences in bilayer thickness and coverage parameters when fitted with a model of the nanoSLB described as a single homogeneous layer (Figure S8 and Table S4). Although the contributions of the headgroups to the overall reflectivity are small, by parametrizing the nanoSLB with the same layout as that used for the flat bilayer (i.e., with separate headgroups and tail regions as shown in Figures S1 and S7, as opposed to the single layer of Figure S8), the respective hydrophilic and hydrophobic regions of the planar and nanoSLB can share a common SLD value imposing an additional constraint on the model. Furthermore, treating the nanoSLB as a single layer does not reduce the number of parameters required to model the data in this case (Tables S3 and S4) and the posterior distributions of the bilayer parameters obtained display a more symmetric distribution when the nanoSLB is parametrized as a conventional lipid bilayer with distinct regions.

Additional Characterization by Off-Specular Neutron Scattering. The NR curves measured in D₂O showed a strong off-specular signal captured in the 2D detector images as horizontal stripes in the region of total reflection (Figure 5A), which caused the intensity dips visible in the specular reflectivity signal below the critical edge (Figure S6, inset). This is similar to that observed in the case of resonators, characterized by a potential well, formed of a region of low SLD in between two regions of high SLD.^{43,44} In the case of the spherical NP system under investigation here, the increasing volume fraction of silicon oxide (SLD of SiO₂ = $3.47 \times 10^{-6} \text{ \AA}^{-2}$) toward the center of the NP monolayer generates a region of low SLD in comparison to the D₂O-rich regions above and below the monolayer center (SLD of D₂O = $6.35 \times 10^{-6} \text{ \AA}^{-2}$), which explains the appearance of the resonances observed. The addition of hPOPC caused both an increase in the intensity of the off-specular scattering and a shift in the Q_z position of the resonances (Figure 5A). Simulations of the off-specular data⁴⁵ reproduced qualitatively the signal change observed for the NP monolayer before and after addition of lipids (Figure 5B) confirming the validity of the specular reflectivity model used to fit the data. The off-specular scattering simulations complemented the GISAXS results indicating higher packing densities in the larger NP arrays. To reproduce the measured off-specular intensities of the 100 and 50 nm particles (Figure S8), micrometer-sized D₂O clusters had to be included in between the NPs in the calculations, while these large D₂O clusters were not required to simulate the signal from the 200 nm particles, indicating the absence of large defects in the monolayer made with the larger particles.

While off-specular reflectometry is sensitive to changes in the SLD distribution over micrometer length scales, GISANS measurements are sensitive to variations of the in-plane SLD distribution over nanometer length scales.⁴⁶ Following up on the GISAXS data collected on the dry NP arrays, the process of nanoSLB formation was investigated by GISANS, which enables measurements of grazing incidence small-angle scattering on buried (e.g., wet) biological thin films. The analysis of the integrated peak positions yielded a correlation distance of 2083 Å prior to the addition of lipids, in line with the values obtained from DLS, GISAXS, and NR (Figure 2). A comparison of the GISANS signals before and after the addition of hPOPC to the NP array in D₂O revealed an increase in the intensity of the overall scattering in the 2D detector image, in line with the increased contrast in the sample caused by the addition of hydrogenous lipids in D₂O (Figure 5C,D). Notably, along with the change in intensity, the adsorbed lipids caused a shift of the maxima positions in Q_y , with a reduction of the average inter-peak separation, resulting in an increase in the relative correlation distance from 2083 to 2167 Å, corresponding to an overall increase of 84 Å in the particle diameter, as calculated from the linear regression of the peak positions (Figure 5E). According to the structural information obtained from the NR data, the total bilayer thickness formed around the NP amounts to ~37 Å; thus, the expected increase in the apparent NP diameter upon bilayer formation would be ~74 Å, close to the 84 Å obtained from the model-free GISANS analysis, which corroborated the NR results.

CONCLUSIONS

The properties of nanoSLBs have been investigated both in bulk^{47–51} and at interfaces^{18,20,24,52} with a wide range of biophysical techniques. Here, we provide a close-up on the molecular structure of coexisting flat and curved lipid bilayers assembled on nanoparticle arrays, using a combination of surface-sensitive imaging and scattering techniques. Together, the data demonstrate the possibility of using large NP arrays assembled via an accessible bottom-up method that does not involve complex nanofabrication, as a substrate for the formation of high-coverage curved lipid bilayers over large surfaces. The combination of scattering and imaging methods granted access to accurate structural information on the vertical and in-plane structure of the nanoSLB, revealing the coexistence of planar and curved regions that displayed different lipid packing between the two arrangements. The nanoSLB platform described here provides a new tool for the study of fundamental and applied aspects of curvature-dependent membrane phenomena, opening new possibilities to investigate curvature-induced lipid phase separation and protein segregation using both grazing incidence neutron scattering coupled with isotopic labeling, as well as more widespread fluorescence-based imaging techniques.

ASSOCIATED CONTENT

Supporting Information

The Supporting Information is available free of charge at <https://pubs.acs.org/doi/10.1021/acsami.2c18956>.

Materials and methods with explanatory figures; description of NP arrays preparation; description of experimental setup for AMF; fluorescence microscopy; DLS, GISAXS, GISANS, and NR; detailed description of NR data modeling; DLS results; Bayesian error analysis of reflectometry fits and corresponding tabulated parameters; GISAXS simulations; additional details on QCMD and fluorescence microscopy measurements; and additional off-specular scattering simulations (PDF)

AUTHOR INFORMATION

Corresponding Authors

Nicolò Paracini – Department for Biomedical Science and Biofilms – Research Center for Biointerfaces, Faculty of Health and Society, Malmö University, 205 06 Malmö, Sweden; orcid.org/0000-0003-3178-4867; Email: nicolo.paracini@mau.se

Marité Cárdenas – Department for Biomedical Science and Biofilms – Research Center for Biointerfaces, Faculty of Health and Society, Malmö University, 205 06 Malmö, Sweden; School of Biological Sciences, Nanyang Technological University, 639798, Singapore; orcid.org/0000-0003-0392-3540; Email: marite.cardenas@mau.se

Authors

Philipp Gutfreund – Institut Laue-Langevin (ILL), 38000 Grenoble, France

Rebecca Welbourn – ISIS Neutron & Muon Source, STFC, Rutherford Appleton Laboratory, Harwell, Oxfordshire OX11 0QX, U.K.; orcid.org/0000-0002-4254-5354

Juan Francisco Gonzalez-Martinez – Department for Biomedical Science and Biofilms – Research Center for Biointerfaces, Faculty of Health and Society, Malmö

University, 205 06 Malmö, Sweden; orcid.org/0000-0001-5518-4095

Kexin Zhu – School of Biological Sciences, Nanyang Technological University, 639798, Singapore

Yansong Miao – School of Biological Sciences, Nanyang Technological University, 639798, Singapore

Nageshwar Yepuri – National Deuteration Facility, Australian Nuclear Science and Technology Organization (ANSTO), Lucas Heights, NSW 2234, Australia

Tamim A. Darwish – National Deuteration Facility, Australian Nuclear Science and Technology Organization (ANSTO), Lucas Heights, NSW 2234, Australia

Christopher Garvey – Heinz Maier-Leibnitz Zentrum (MLZ), Technische Universität München, 85748 Garching, Germany; orcid.org/0000-0001-6496-7008

Sarah Waldie – Department for Biomedical Science and Biofilms – Research Center for Biointerfaces, Faculty of Health and Society, Malmö University, 205 06 Malmö, Sweden

Johan Larsson – Department for Biomedical Science and Biofilms – Research Center for Biointerfaces, Faculty of Health and Society, Malmö University, 205 06 Malmö, Sweden

Max Wolff – Department of Physics and Astronomy, Uppsala University, 751 20 Uppsala, Sweden; orcid.org/0000-0002-7517-8204

Complete contact information is available at:
<https://pubs.acs.org/10.1021/acsami.2c18956>

Notes

The authors declare no competing financial interest.

ACKNOWLEDGMENTS

M.C. and N.P. thank the Swedish Research Council for financial support. N.P. acknowledges support from Nordforsk – Nordic Neutron Science Program (Grant 106881). M.C. thanks Wennergren foundation for financial support. The authors thank the ILL for beamtime (D22: doi:10.5291/ILL-DATA.8-02-912, FIGARO: doi:10.5291/ILL-DATA.8-02-889) and Prof. Jaume Torres for access to a Langmuir Trough at Nanyang Technological University. This study was supported by Singapore MOE Tier 3 (MOE2019-T3-1-012) to Y.M. The National Deuteration Facility in Australia is partly funded by The National Collaborative Research Infrastructure Strategy (NCRIS), an Australian Government initiative. M.C. and M.W. thank the Röntgen-Ångström Cluster, grant no. 2021-05963.

ABBREVIATIONS

NP, nanoparticles
SLB, supported lipid bilayer
nanoSLB, nanoparticle-supported lipid bilayer
SLD, scattering length density
NR, neutron reflectometry
GISAXS, grazing incidence small-angle X-ray scattering
GISANS, grazing incidence small-angle neutron scattering
FRAP, fluorescence recovery after photobleaching
QCMD, quartz crystal microbalance with dissipation
AFM, atomic force microscopy
TIRF, total internal reflection fluorescence
DLS, dynamic light scattering

REFERENCES

- (1) Clifton, L. A.; Campbell, R. A.; Sebastiani, F.; Campos-Terán, J.; Gonzalez-Martinez, J. F.; Björklund, S.; Sotres, J.; Cárdenas, M. Design and Use of Model Membranes to Study Biomolecular Interactions Using Complementary Surface-Sensitive Techniques. *Adv. Colloid Interface Sci.* **2020**, *277*, No. 102118.
- (2) Santoro, F.; Lubrano, C.; Matrone, G. M.; Iaconis, G. New Frontiers for Selective Biosensing with Biomembrane-Based Organic Transistors. *ACS Nano* **2020**, *14*, 12271–12280.
- (3) Hardy, G. J.; Nayak, R.; Zauscher, S. Model Cell Membranes: Techniques to Form Complex Biomimetic Supported Lipid Bilayers via Vesicle Fusion. *Curr. Opin. Colloid Interface Sci.* **2013**, *18*, 448–458.
- (4) Tabaei, S. R.; Choi, J.-H.; Haw Zan, G.; Zhdanov, V. P.; Cho, N.-J. Solvent-Assisted Lipid Bilayer Formation on Silicon Dioxide and Gold. *Langmuir* **2014**, *30*, 10363–10373.
- (5) Kurniawan, J.; Ventrici De Souza, J. F.; Dang, A. T.; Liu, G. Y.; Kuhl, T. L. Preparation and Characterization of Solid-Supported Lipid Bilayers Formed by Langmuir-Blodgett Deposition: A Tutorial. *Langmuir* **2018**, *34*, 15622–15639.
- (6) Paracini, N.; Clifton, L. A.; Skoda, M. W. A.; Lakey, J. H. Liquid Crystalline Bacterial Outer Membranes Are Critical for Antibiotic Susceptibility. *Proc. Natl. Acad. Sci. U.S.A.* **2018**, *115*, No. 201803975.
- (7) Hsieh, W.-T.; Hsu, C.-J.; Capraro, B. R.; Wu, T.; Chen, C.-M.; Yang, S.; Baumgart, T. Curvature Sorting of Peripheral Proteins on Solid-Supported Wavy Membranes. *Langmuir* **2012**, *28*, 12838–12843.
- (8) Beltrán-Heredia, E.; Tsai, F. C.; Salinas-Almaguer, S.; Cao, F. J.; Bassereau, P.; Monroy, F. Membrane Curvature Induces Cardiolipin Sorting. *Commun. Biol.* **2019**, *2*, 225.
- (9) McMahon, H. T.; Boucrot, E. Membrane Curvature at a Glance. *J. Cell Sci.* **2015**, *128*, 1065–1070.
- (10) Ramamurthi, K. S. Protein Localization by Recognition of Membrane Curvature. *Curr. Opin. Microbiol.* **2010**, *13*, 753–757.
- (11) Ramamurthi, K. S.; Losick, R. Negative Membrane Curvature as a Cue for Subcellular Localization of a Bacterial Protein. *Proc. Natl. Acad. Sci. U.S.A.* **2009**, *106*, 13541–13545.
- (12) Renner, L. D.; Weibel, D. B. Cardiolipin Microdomains Localize to Negatively Curved Regions of Escherichia Coli Membranes. *Proc. Natl. Acad. Sci. U.S.A.* **2011**, *108*, 6264–6269.
- (13) Kawai, F.; Shoda, M.; Harashima, R.; Sadaie, Y.; Hara, H.; Matsumoto, K. Cardiolipin Domains in Bacillus Subtilis Marburg Membranes. *J. Bacteriol.* **2004**, *186*, 1475–1483.
- (14) Ikon, N.; Ryan, R. O. Cardiolipin and Mitochondrial Cristae Organization. *Biochim. Biophys. Acta* **2017**, *1859*, 1156–1163.
- (15) Elmer-Dixon, M. M.; Hoody, J.; Steele, H. B.; Becht, D. C.; Bowler, B. E. Cardiolipin Preferentially Partitions to the Inner Leaflet of Mixed Lipid Large Unilamellar Vesicles. *J. Phys. Chem. B* **2019**, *123*, 9111–9122.
- (16) Elmer-Dixon, M. M.; Xie, Z.; Alverson, J. B.; Priestley, N. D.; Bowler, B. E. Curvature-Dependent Binding of Cytochrome c to Cardiolipin. *J. Am. Chem. Soc.* **2020**, *142*, 19532–19539.
- (17) Pyrshev, K.; Yesylevsky, S.; Bogdanov, M. TTAPE-Me Dye Is Not Selective to Cardiolipin and Binds to Common Anionic Phospholipids Nonspecifically. *Biophys. J.* **2021**, *120*, 3776–3786.
- (18) Sundh, M.; Svedhem, S.; Sutherland, D. S. Formation of Supported Lipid Bilayers at Surfaces with Controlled Curvatures: Influence of Lipid Charge. *J. Phys. Chem. B* **2011**, *115*, 7838–7848.
- (19) Parthasarathy, R.; Yu, C.; Groves, J. T. Curvature-Modulated Phase Separation in Lipid Bilayer Membranes. *Langmuir* **2006**, *22*, 5095–5099.
- (20) Black, J. C.; Cheney, P. P.; Campbell, T.; Knowles, M. K. Membrane Curvature Based Lipid Sorting Using a Nanoparticle Patterned Substrate. *Soft Matter* **2014**, *10*, 2016–2023.
- (21) Vasilca, V.; Sadeghpour, A.; Rawson, S.; Hawke, L. E.; Baldwin, S. A.; Wilkinson, T.; Bannister, D.; Postis, V. L. G.; Rappolt, M.; Muench, S. P.; Jeuken, L. J. C. Spherical-Supported Membranes as Platforms for Screening against Membrane Protein Targets. *Anal. Biochem.* **2018**, *549*, 58–65.

- (22) Sanii, B.; Smith, A. M.; Butti, R.; Brozell, A. M.; Parikh, A. N. Bending Membranes on Demand: Fluid Phospholipid Bilayers on Topographically Deformable Substrates. *Nano Lett.* **2008**, *8*, 866–871.
- (23) Dabkowska, A. P.; Niman, C. S.; Piret, G.; Persson, H.; Wacklin, H. P.; Linke, H.; Prinz, C. N.; Nylander, T. Fluid and Highly Curved Model Membranes on Vertical Nanowire Arrays. *Nano Lett.* **2014**, *14*, 4286–4292.
- (24) Roiter, Y.; Ornatska, M.; Rammohan, A. R.; Balakrishnan, J.; Heine, D. R.; Minko, S. Interaction of Nanoparticles with Lipid Membrane. *Nano Lett.* **2008**, *8*, 941–944.
- (25) Vegso, K.; Siffalovic, P.; Jergel, M.; Weis, M.; Benkovicova, M.; Majkova, E.; Luby, S.; Kocsis, T.; Capek, I. Silver Nanoparticle Monolayer-to-Bilayer Transition at the Air/Water Interface as Studied by the GISAXS Technique: Application of a New Paracrystal Model. *Langmuir* **2012**, *28*, 9395–9404.
- (26) Wu, L.; Wang, X.; Wang, G.; Chen, G. In Situ X-Ray Scattering Observation of Two-Dimensional Interfacial Colloidal Crystallization. *Nat. Commun.* **2018**, *9*, No. 1335.
- (27) Guo, Y.; Tang, D.; Du, Y.; Liu, B. Controlled Fabrication of Hexagonally Close-Packed Langmuir–Blodgett Silica Particulate Monolayers from Binary Surfactant and Solvent Systems. *Langmuir* **2013**, *29*, 2849–2858.
- (28) Vorobiev, A.; Paracini, N.; Cárdenas, M.; Wolff, M. II-GISANS: Probing Lateral Structures with a Fan Shaped Beam. *Sci. Rep.* **2021**, *11*, No. 17786.
- (29) Müller-Buschbaum, P. Grazing Incidence Small-Angle Neutron Scattering: Challenges and Possibilities. *Polym. J.* **2013**, *45*, 34–42.
- (30) Siffalovic, P.; Majkova, E.; Jergel, M.; Vegso, K.; Weis, M.; Luby, S. Self-Assembly of Nanoparticles at Solid and Liquid Surfaces. In *Smart Nanoparticles Technology*; InTech, 2012.
- (31) Hrubý, J.; Santana, V. T.; Kostiuik, D.; Bouček, M.; Lenz, S.; Kern, M.; Šiffalovič, P.; van Slageren, J.; Neugebauer, P. A Graphene-Based Hybrid Material with Quantum Bits Prepared by the Double Langmuir–Schaefer Method. *RSC Adv.* **2019**, *9*, 24066–24073.
- (32) Renaud, G.; Lazzari, R.; Leroy, F. Probing Surface and Interface Morphology with Grazing Incidence Small Angle X-Ray Scattering. *Surf. Sci. Rep.* **2009**, *64*, 255–380.
- (33) Pospelov, G.; Van Herck, W.; Burle, J.; Carmona Loaiza, J. M.; Durniak, C.; Fisher, J. M.; Ganeva, M.; Yurov, D.; Wuttke, J. BornAgain: Software for Simulating and Fitting Grazing-Incidence Small-Angle Scattering. *J. Appl. Crystallogr.* **2020**, *53*, 262–276.
- (34) Steinmetz, N. F.; Bock, E.; Richter, R. P.; Spatz, J. P.; Lomonosoff, G. P.; Evans, D. J. Assembly of Multilayer Arrays of Viral Nanoparticles via Biospecific Recognition: A Quartz Crystal Microbalance with Dissipation Monitoring Study. *Biomacromolecules* **2008**, *9*, 456–462.
- (35) Seantier, B.; Breffa, C.; Félix, O.; Decher, G. Dissipation-Enhanced Quartz Crystal Microbalance Studies on the Experimental Parameters Controlling the Formation of Supported Lipid Bilayers. *J. Phys. Chem. B* **2005**, *109*, 21755–21765.
- (36) Richter, R. P.; Bérat, R.; Brisson, A. R. Formation of Solid-Supported Lipid Bilayers: An Integrated View. *Langmuir* **2006**, *22*, 3497–3505.
- (37) Richter, R.; Mukhopadhyay, A.; Brisson, A. Pathways of Lipid Vesicle Deposition on Solid Surfaces: A Combined QCM-D and AFM Study. *Biophys. J.* **2003**, *85*, 3035.
- (38) Mornet, S.; Lambert, O.; Dugué, E.; Brisson, A. The Formation of Supported Lipid Bilayers on Silica Nanoparticles Revealed by Cryoelectron Microscopy. *Nano Lett.* **2005**, *5*, 281–285.
- (39) Armanious, A.; Gerelli, Y.; Micciulla, S.; Pace, H. P.; Welbourn, R. J. L.; Sjöberg, M.; Agnarsson, B.; Höök, F. Probing the Separation Distance between Biological Nanoparticles and Cell Membrane Mimics Using Neutron Reflectometry with Sub-Nanometer Accuracy. *J. Am. Chem. Soc.* **2022**, *144*, 20726–20738.
- (40) Luchini, A.; Nzulumike, A. N. O.; Lind, T. K.; Nylander, T.; Barker, R.; Arleth, L.; Mortensen, K.; Cárdenas, M. Towards Biomimics of Cell Membranes: Structural Effect of Phosphatidylino-sitol Triphosphate (PIP3) on a Lipid Bilayer. *Colloids Surf., B* **2019**, *173*, 202–209.
- (41) Åkesson, A.; Lind, T.; Ehrlich, N.; Stamou, D.; Wacklin, H.; Cárdenas, M. Composition and Structure of Mixed Phospholipid Supported Bilayers Formed by POPC and DPPC. *Soft Matter* **2012**, *8*, 5658.
- (42) Schmiedel, H.; Almásy, L.; Klose, G. Multilamellarity, Structure and Hydration of Extruded POPC Vesicles by SANS. *Eur. Biophys. J.* **2006**, *35*, 181–189.
- (43) Perrichon, A.; Devishvili, A.; Komander, K.; Pálsson, G. K.; Vorobiev, A.; Lavén, R.; Karlsson, M.; Wolff, M. Resonant Enhancement of Grazing Incidence Neutron Scattering for the Characterization of Thin Films. *Phys. Rev. B* **2021**, *103*, No. 235423.
- (44) Feng, Y. P.; Sinha, S. K.; Deckman, H. W.; Hastings, J. B.; Siddons, D. P. X-Ray Flux Enhancement in Thin-Film Waveguides Using Resonant Beam Couplers. *Phys. Rev. Lett.* **1993**, *71*, 537–540.
- (45) Hafner, A.; Gutfreund, P.; Toperverg, B. P.; Jones, A. O. F.; de Silva, J. P.; Wildes, A.; Fischer, H. E.; Geoghegan, M.; Sferrazza, M. Combined Specular and Off-Specular Reflectometry: Elucidating the Complex Structure of Soft Buried Interfaces. *J. Appl. Crystallogr.* **2021**, *54*, 924–948.
- (46) Müller-Buschbaum, P. Grazing Incidence Small-Angle Neutron Scattering: Challenges and Possibilities. *Polym. J.* **2013**, *45*, 34–42.
- (47) Savarala, S.; Ahmed, S.; Ilies, M. A.; Wunder, S. L. Formation and Colloidal Stability of DMPC Supported Lipid Bilayers on SiO₂ Nanobeads. *Langmuir* **2010**, *26*, 12081–12088.
- (48) Drazenovic, J.; Ahmed, S.; Tuzinkiewicz, N.-M.; Wunder, S. L. Lipid Exchange and Transfer on Nanoparticle Supported Lipid Bilayers: Effect of Defects, Ionic Strength, and Size. *Langmuir* **2015**, *31*, 721–731.
- (49) Ahmed, S.; Nikolov, Z.; Wunder, S. L. Effect of Curvature on Nanoparticle Supported Lipid Bilayers Investigated by Raman Spectroscopy. *J. Phys. Chem. B* **2011**, *115*, 13181–13190.
- (50) Tanaka, M.; Komikawa, T.; Yanai, K.; Okochi, M. Proteomic Exploration of Membrane Curvature Sensors Using a Series of Spherical Supported Lipid Bilayers. *Anal. Chem.* **2020**, *92*, 16197–16203.
- (51) Luchini, A.; Vitiello, G. Understanding the Nano-Bio Interfaces: Lipid-Coatings for Inorganic Nanoparticles as Promising Strategy for Biomedical Applications. *Front. Chem.* **2019**, *7*, 343.
- (52) Brozell, A. M.; Muha, M. A.; Sanii, B.; Parikh, A. N. A Class of Supported Membranes: Formation of Fluid Phospholipid Bilayers on Photonic Band Gap Colloidal Crystals. *J. Am. Chem. Soc.* **2006**, *128*, 62–63.